Supporting Information

Multi-Angle Tracking Synthetic Kinetics of of Phase Evolution in Li-Rich Mn-Based Cathodes

Shenyang Xu[1], Zhefeng Chen[1], Wenguang Zhao[1], Wenju Ren[1,2]，Chenxin Hou[1], Jiajie Liu[1], Wu Wang[3], Chong Yin[4], Xinghua Tan[1], Xiaobing Lou[5], Xiangming Yao[1], Zhihai Gao[1], Hao Liu[6], Lu Wang[1], Zuwei Yin[1], Bao Qiu[7], Bingwen Hu[5], Tianyi Li[8,]*, Cheng Dong[1], Feng Pan[1,]*, Mingjian Zhang[9,]**
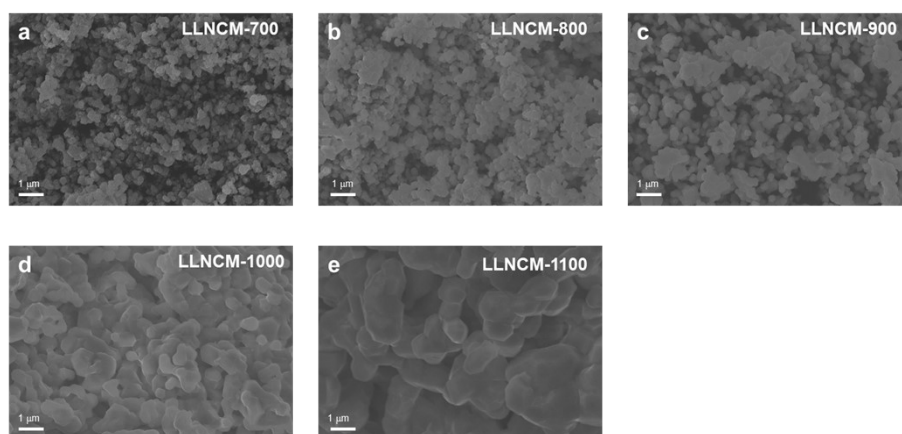
Figure S1. SEM images of LLNCM-700 (a), LLNCM-800 (b), LLNCM-900 (c), LLNCM-1000 (d) and LLNCM-1100 (e).
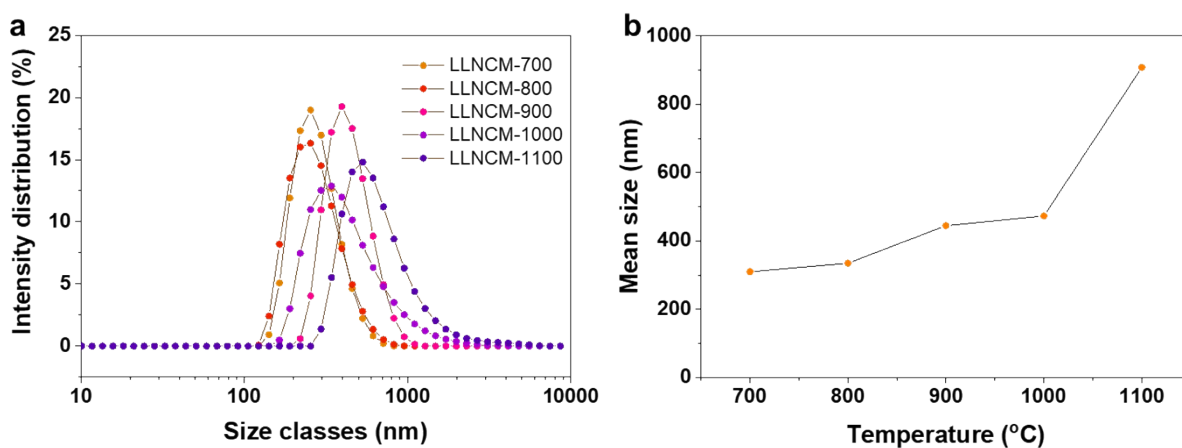
Figure S2. Particle size distributions (a) and average particle sizes (b) of LLNCM-700, LLNCM-800, LLNCM-900, LLNCM-1000 and LLNCM-1100 cathodes, obtained by the zeta potential method.

To determine the particle size and distribution of different samples, we performed SEM tests and also adopted a Nano-ZS90 zeta potential analyzer (The same mass of powder was dispersed in ethanol and sonicated for 20 min, and the upper suspension was taken for testing). As shown in Figure S1-2, LLNCM-700 and LLNCM-800 showed the similar particle size distribution with a center as 300 nm. When the temperature went up to 900 and 1000 °C, the particle size gradually increased to 400-500 nm (LLNCM-900 and LLNCM-1000). When the temperature was further increased to 1100 °C, further merging among particles was clearly observed, leading to the larger average particle size (~1 μm).
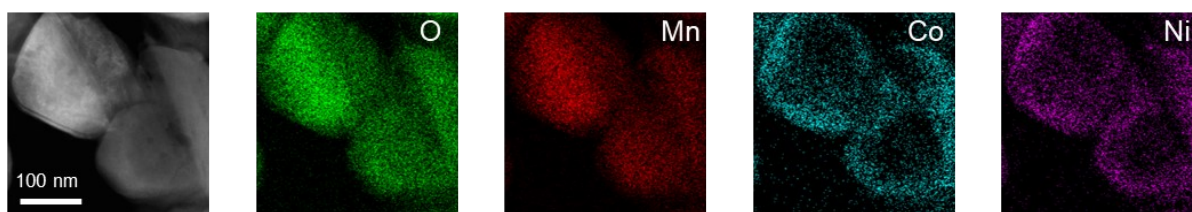

Figure S3. *Ex-situ* TEM images and the corresponding EDX spectra of Li, Mn, Co, and Ni of LLNCM-700.
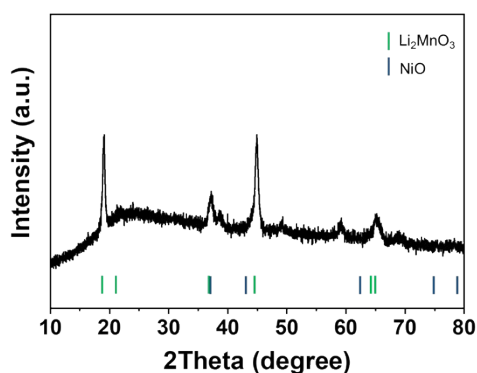

Figure S4. The XRD of precursor.

The formation temperatures of the two phases, C2/m and R-3m, significantly affect the element distribution. Previous reports indicate that Li_2MnO_3 forms at 450°C,[1] as evidenced by the XRD pattern of the precursor, which exhibits a Li_2MnO_3 phase with superlattice peaks (Figure S4). On the other hand, $Li[Ni_{1/3}Co_{1/3}Mn_{1/3}]O_2$ is typically synthesized at temperatures ranging from 800-900 °C,[2-4] resulting in an initial non-uniform distribution of the different transition metal elements, namely, elemental segregation of transition metals. That is consistent with previous work.[5] As temperature further increases, phase fusion begins. As discussed in our

manuscript, this process gradually leads to more uniform elemental distribution, transitioning from particle level to nanodomain level, and ultimately to local structure level, ensuring improved homogeneity.

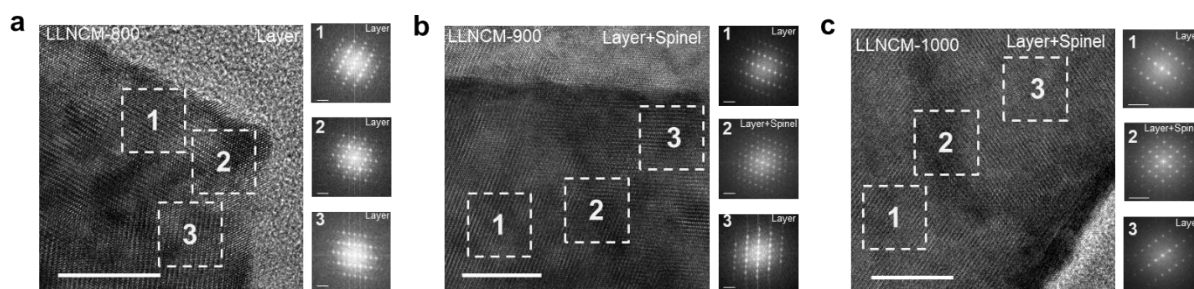**Figure S5.** HRTEM images of LLNCM-800 (a), LLNCM-900 (b), and LLNCM-1000 (c) at the surface. The FFT maps are deduced from the corresponding regions. The scale bars in HRTEM images and FFT maps are 10 nm and 2 1/nm, respectively.
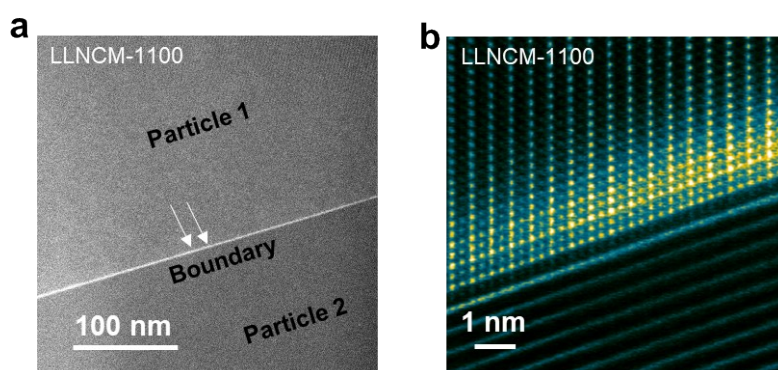
Figure S6. Boundary in LLNCM-1100 (a) and corresponding HAADF-STEM images of boundary (b).

Figure S7. HRTEM image (a) and the corresponding SAED patterns (b, c) of LLNCM-1000.
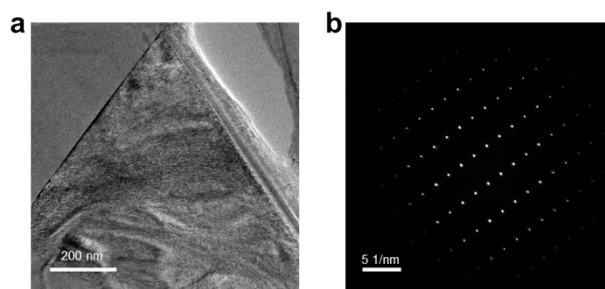
Figure S8. HRTEM image (a) and SAED pattern (b) of LLNCM-1100.
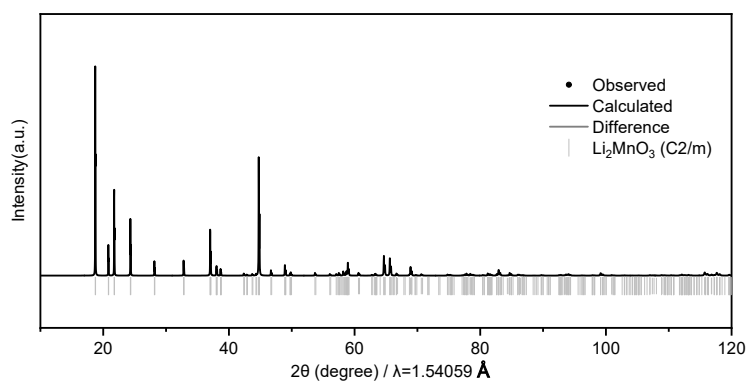
Figure S9. The simulated XRD pattern of Li_2MnO_3 ($C2/m$).
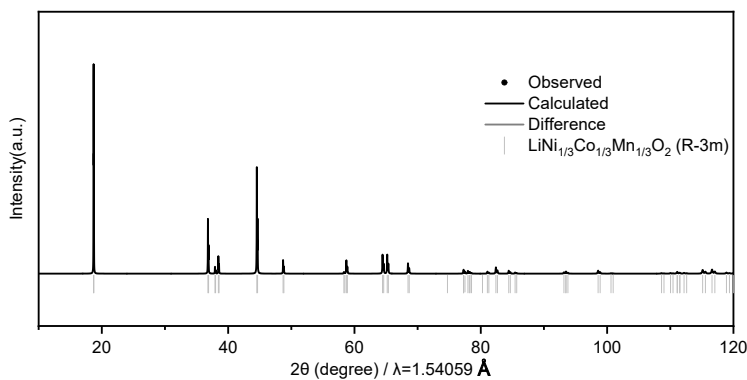
Figure S10. The simulated XRD pattern of $LiNi_{1/3}Co_{1/3}Mn_{1/3}O_2$ (R-$3m$).
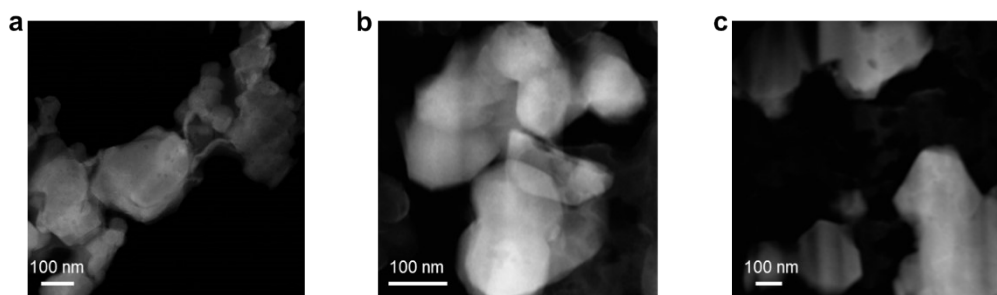
Figure S11. *Ex-situ* STEM images of LLNCM-700 (a), LLNCM-800 (b), LLNCM-900 (c).
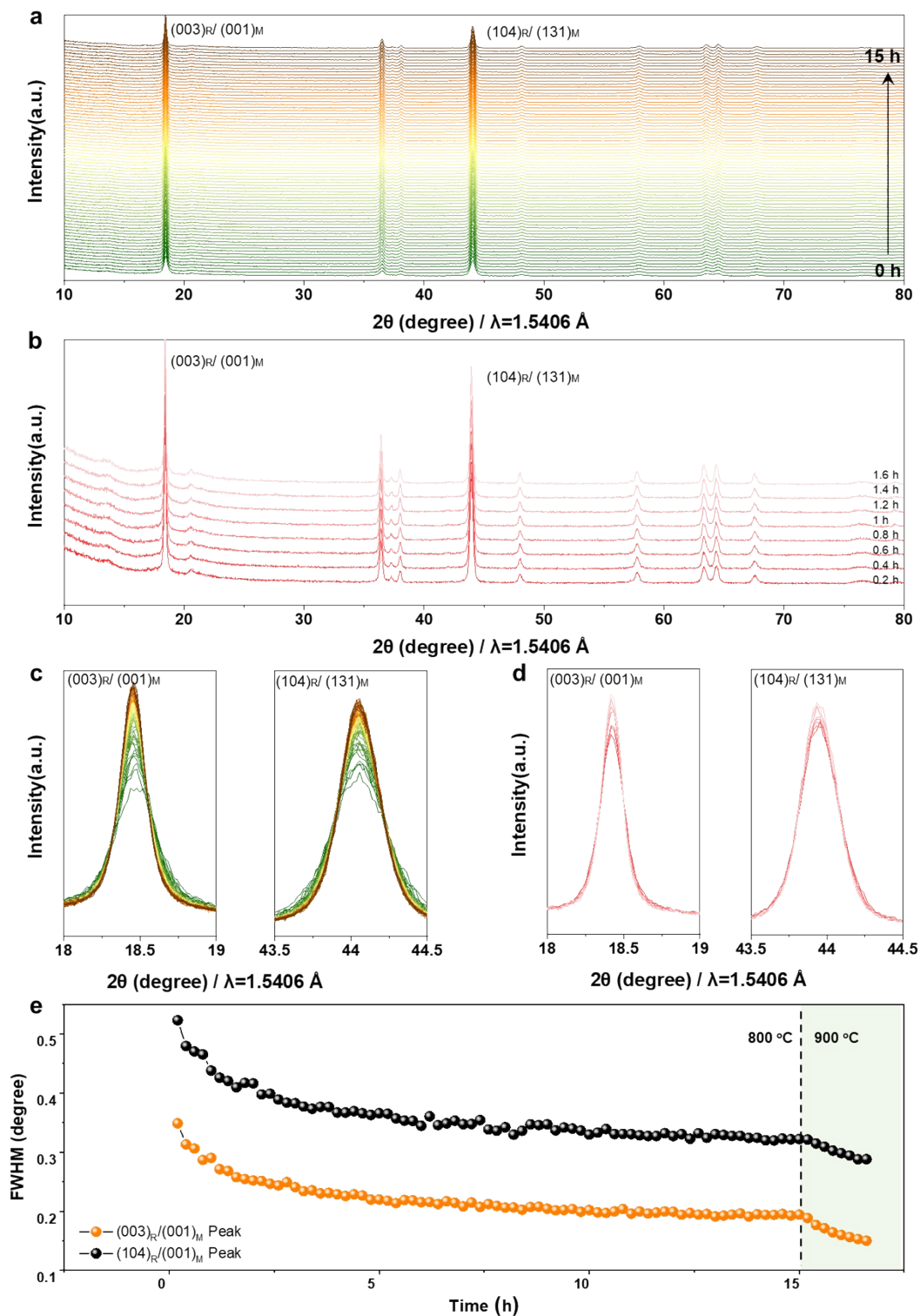
Figure S12. (a) *In-situ* XRD patterns collected when holding at 800 °C for 15 hours. (b) *In-situ* XRD patterns collec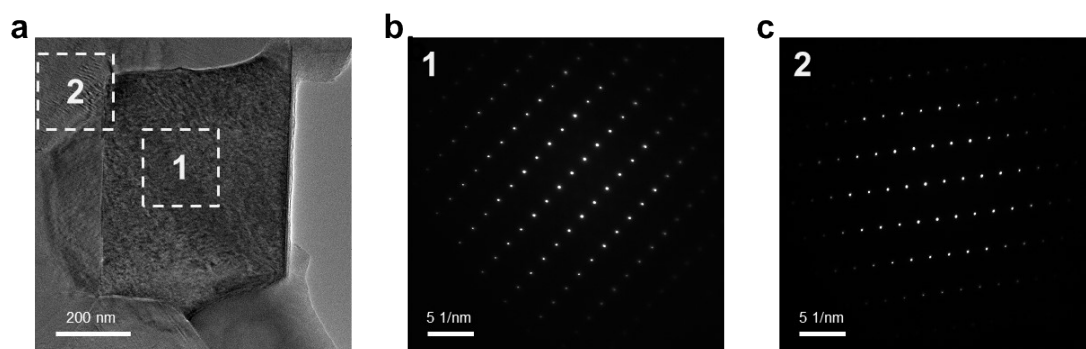ted when further heating the material to 900 °C after 800 °C holding . (c) The enlarged $(003)_R/(001)_M$ and $(104)_R/(131)_M$ peaks from (a). (d) The enlarged $(003)_R/(001)_M$ and $(104)_R/(131)_M$ peaks from (b). (e) The corresponding FWHM values as functions of the holding time.

5
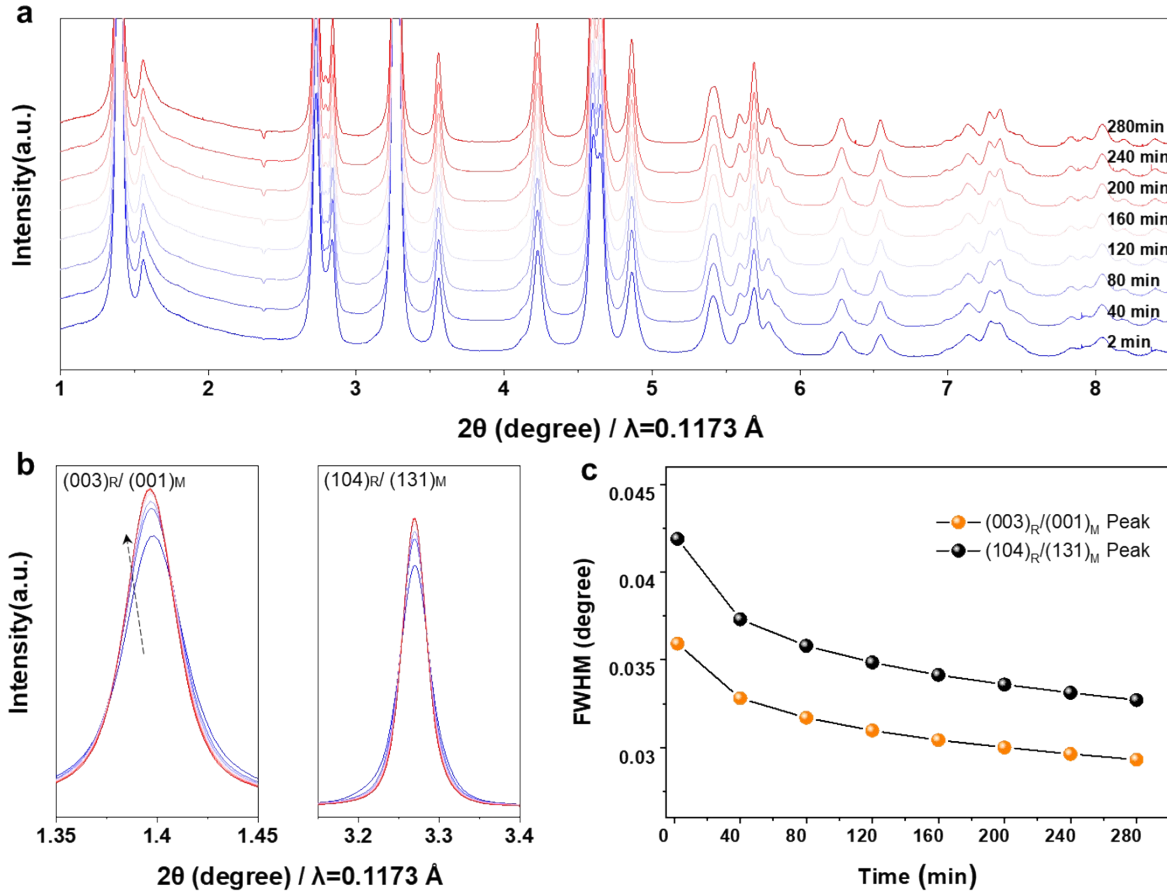
Figure S13. (a) *In-situ* XRD patterns collected when holding at 1000 °C for 280 mins. (b) The enlarged (003) and (104) peaks. (c) The corresponding FWHM changes with the holding time.

In-situ XRD test was carried out when calcined at 800 °C for 15 hours. As shown in Figure S12, the full width at half maximum (FWHM) of the main diffraction peaks $(003)_R/(001)_M$ and $(104)_R/(131)_M$ quickly decreased and gradually stabilized after about 5 hours, suggesting the material reached a relative stable state. Another similar experiment was performed at 1000 °C (Figure S13) and revealed a similar trend. It indicates that the calcination time mainly affects the structure in the first several hours. Our previous work proved that the weight loss during cathode preparation is very small after 5 hours.[6] Furthermore, the temperature was further elevated to 900°C after 800 °C holding, dramatic decreases in the FWHM of the main peaks were observed (Figure S12). This confirms that temperature has a much more pronounced effect on the structural evolution of lithium-rich transition metal oxides compared to the extended holding time. Collectively, these *in-situ* analyses demonstrate that for lithium-rich materials, temperature exerts a stronger influence over structural changes than prolonged heating duration (> 5 hours). In the manuscript, all calcination times at different temperatures are longer than 5

hours, in this case, the temperature will be the dominant factor for the structure changes. It is rational that we labelled the samples as LLNCM-700, LLNCM-800, LLNCM-900, LLNCM-1000 and LLNCM-1100 using the individual temperature. The findings provide useful guidance for optimizing synthesis protocols, suggesting that more attention should be paid to temperature control rather than simply extending holding time.
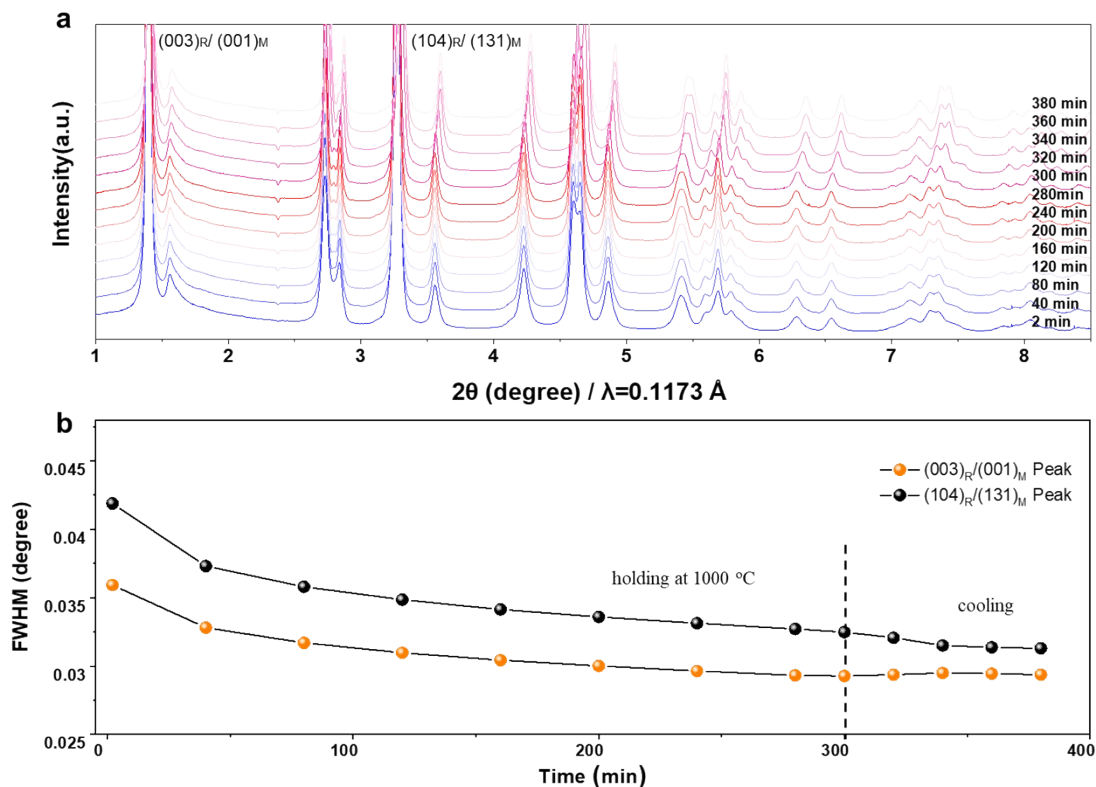
Figure S14. (a) *In-situ* XRD patterns collected when holding at 1000 °C for 5 hours and naturally cooling to room temperature. (b) The corresponding FWHM values of The $(003)_R/(001)_M$ and $(104)_R/(131)_M$ peaks as functions of time.

As shown in Figure S14, the effect of cooling on the peak FWHM is assessed. The changes in the FWHM values are minor before and after cooling. The *in-situ* XRD patterns when heating to 1000°C and the corresponding FWHM variations also are provided (Figure S15). It presents the similar trend with the *ex-situ* XRD results in Figure 3.
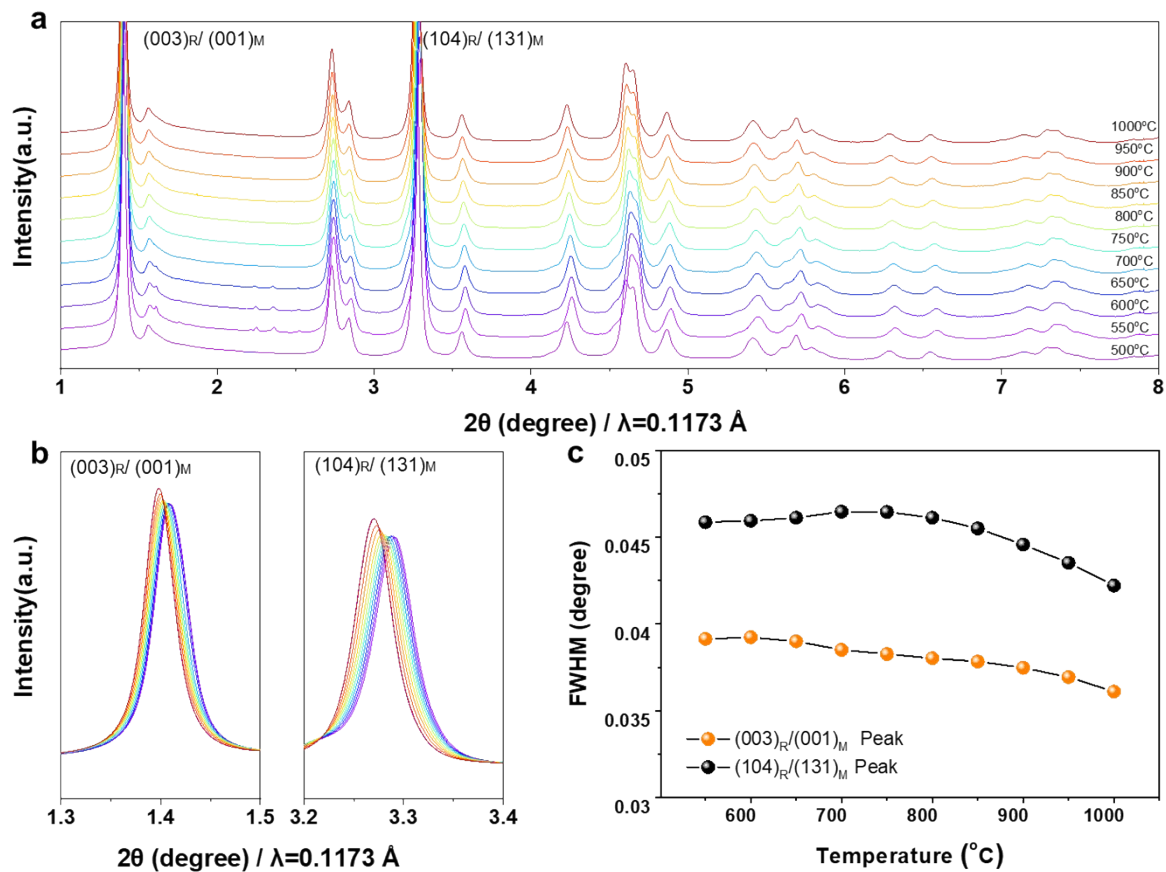
Figure S15. (a) *In-situ* XRD patterns collected when heating the precursor to 1000 °C. (b) The enlarged $(003)_R/(001)_M$ and $(104)_R/(131)_M$ peaks. (c) The corresponding FWHM values as functions of the holding time.
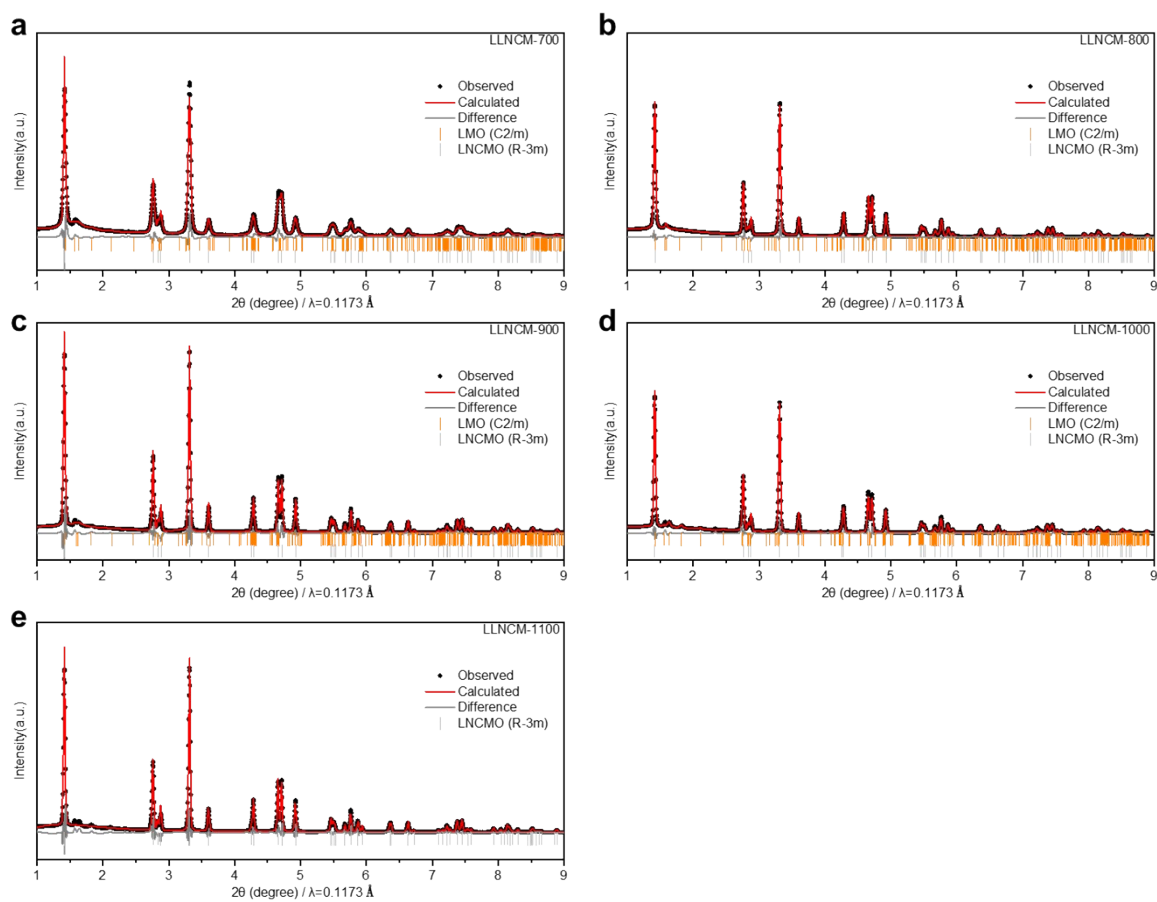
Figure S16. Rietveld refinement results of XRD patterns for LLNCM-700 (a), LLNCM-800 (b), LLNCM-900 (c), LLNCM-1000 (d) and LLNCM-1100 (e).
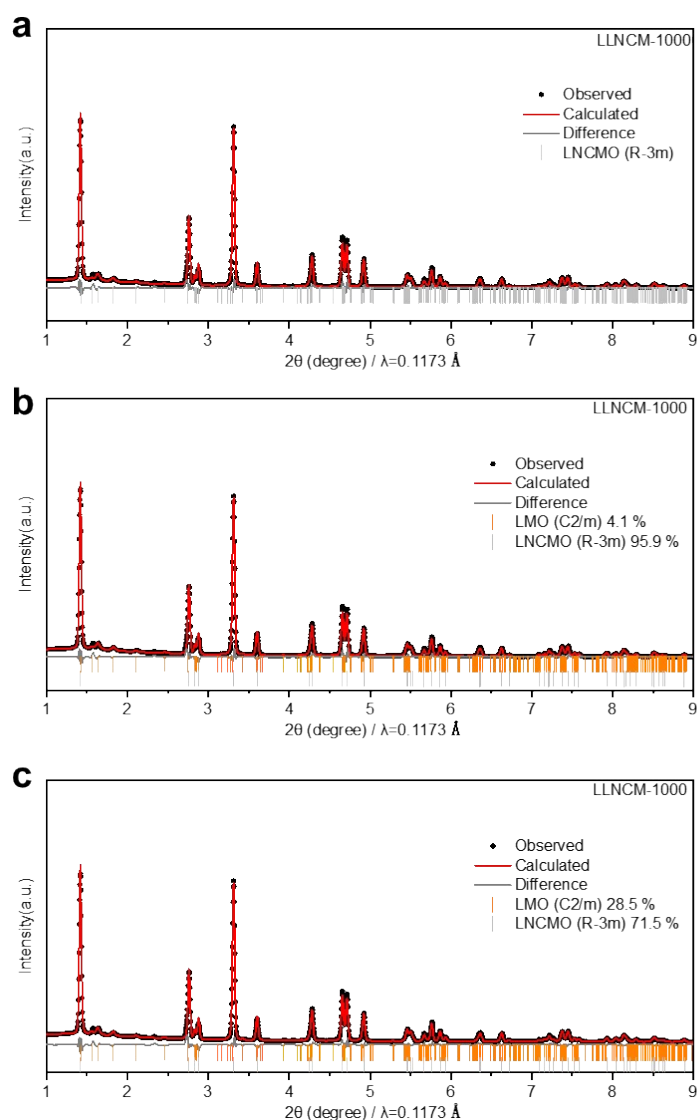
Figure S17. Rietveld refinement results of XRD patterns for different condition of LLNCM-1000.

The purpose of XRD refinement is to show that refinement cannot quantify the contents of two phases precisely due to the very similar structures of the two phases. We list the refinement process and parameters involved as follows:

(1) Strictly control the background using a Chebyshev polynomial (order: 7) and correct the zero point.

(2) Refine the unit cell parameters.

(3) Use the PV_TCHZ model for peak type refinement.

(4) Refine B-factors with the constraints of being all positive and having the same occupancy for atoms at the same site.

(5) Consider the possibility of partial antisite occupancy for transition metals when refining atomic occupancies.

(6) Only refine the atomic positions of non-fractionally occupied oxygen atoms, which will have a limited impact on the results. Keep the positions of other atoms fixed.

Three different refinements for XRD pattern of LLNCM-1000 can give good fitting results and very similar *Rwp* values but very different phase fractions. It indicates that the phase composition can not be exactly determined by the Rietveld refinement due to the high-degree phase fusion. In this case, local and short-range structure changes would dominate the microscopic structure changes as the temperature increases.
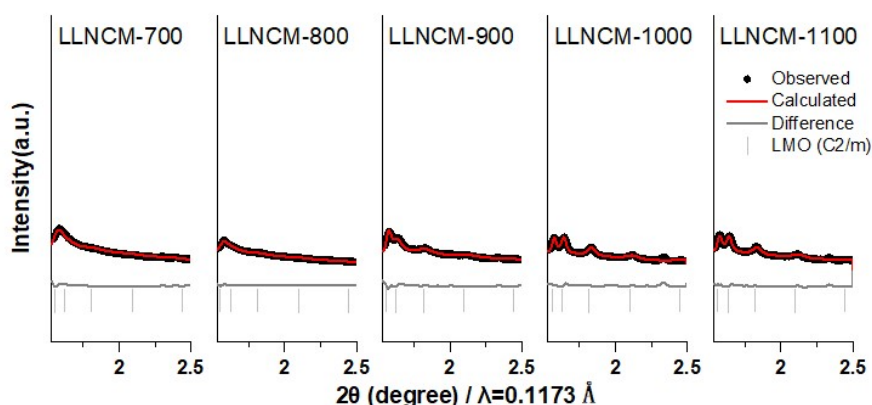
Figure S18. Staking faults refinement results of LLNCM-700, LLNCM-800, LLNCM-900, LLNCM-1000 and LLNCM-1100 cathodes.
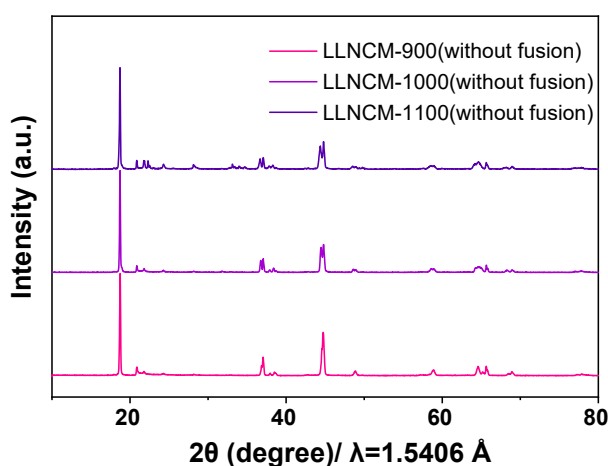
Figure S19. The raw XRD data of experiments at different temperatures based on this without fusion tableting method.
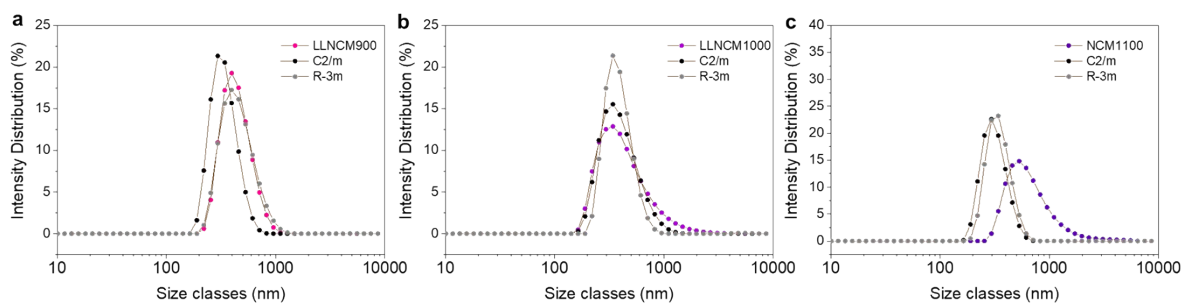
Figure S20. Comparison of particle size distribution of NCM111 and Li$_2$MnO$_3$ and LLNCM materials at corresponding temperatures ((a) 900 ^{o}C, (b) 1000 ^{o}C, (c) 1100 ^{o}C).
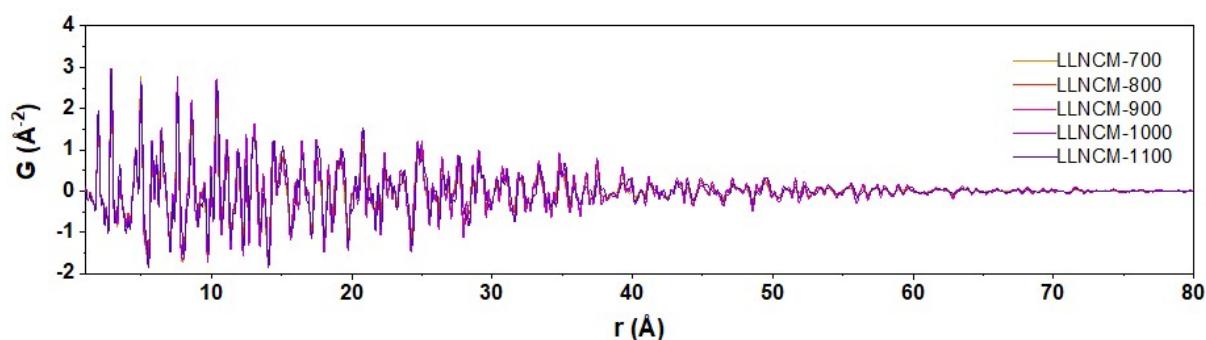
Figure S21 The synchrotron X-ray total scattering data of LLNCM-700, LLNCM-800, LLNCM-900, LLNCM-1000 and LLNCM-1100.
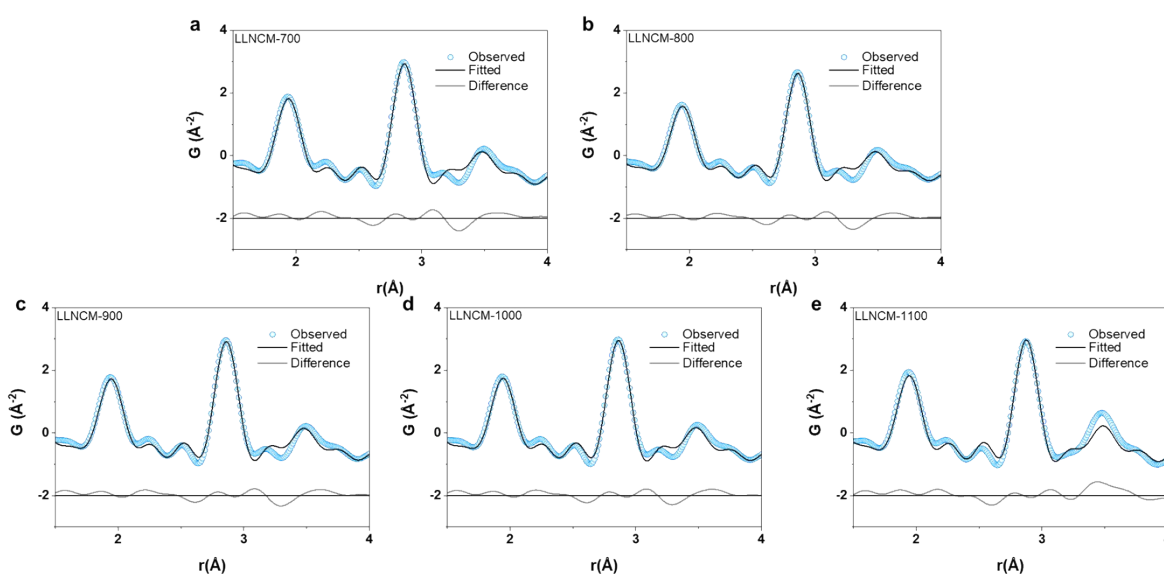
Figure S22. PDF fitting of LLNCM-700, LLNCM-800, LLNCM-900, LLNCM-1000 and LLNCM-1100 cathodes.

Based on the distribution of TM and O in the monoclinic and rhombohedral structures, the peak at around 3.2 Å is mainly attributed to the second nearest neighbor "O-O" pair, while the peak at 3.5 Å is attributed to the second nearest neighbor "TM-O" pair. By fitting the PDF results of LLNCM-700, LLNCM-800, LLNCM-900, LLNCM-1000 and LLNCM-1100 cathodes, we found that this changes in the peak intensity of these two peaks were mainly due to the variations in lattice parameters and oxygen positions (Table S6-7).
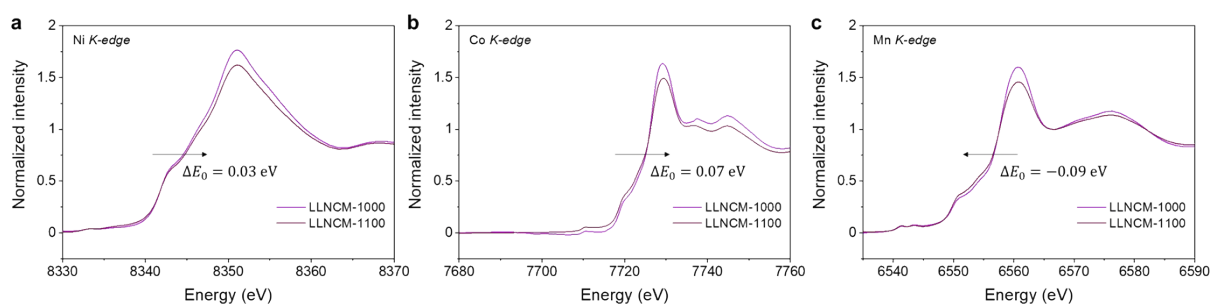
Figure S23. Ni K-edge (a), Co K-edge (b), and Mn K-edge (c) XANES spectra of LLNCM-1000 and LLNCM-1100.
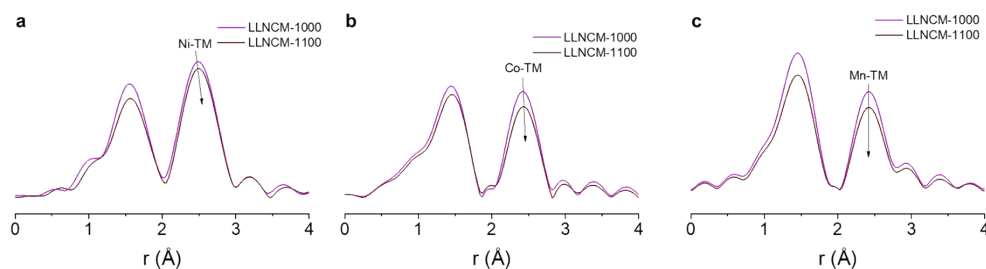
Figure S24. Ni K-edge (a), Co K-edge (b), and Mn K-edge (c) EXAFS spectra of LLNCM-1000 and LLNCM-1100.

The reduced TM-Mn intensity in Figure S24c can be attributed to the decreased valence state.
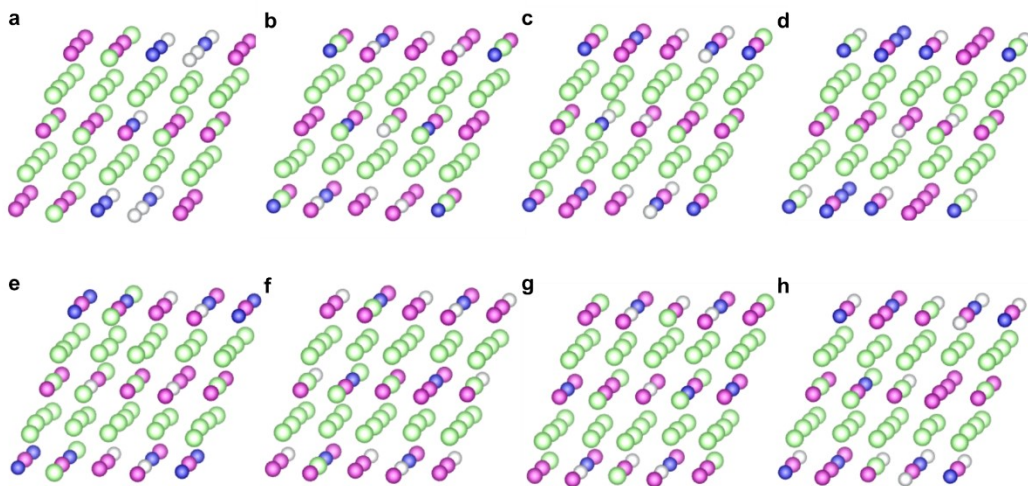
Figure S25. 8 structure models with medium degree of phase fusion constructed by SQS.
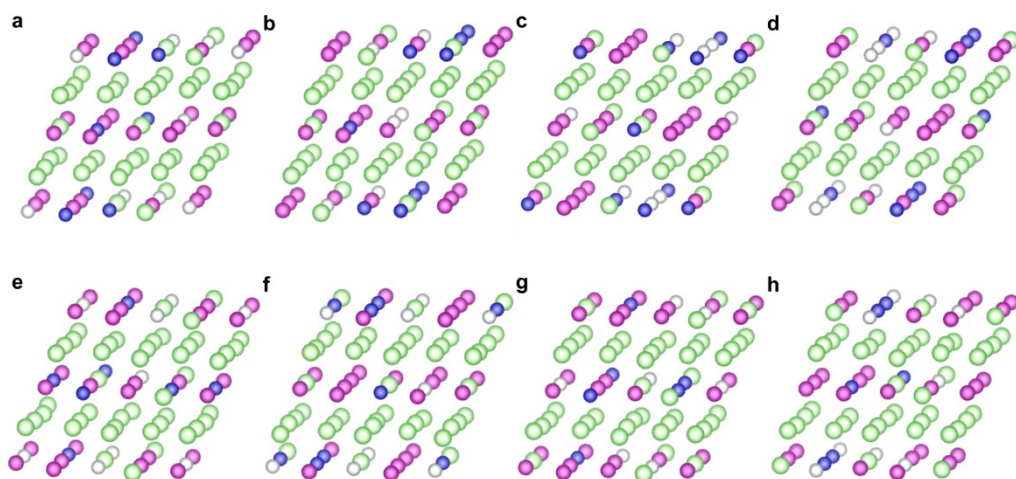
Figure S26. 8 structure models with high degree of phase fusion constructed by SQS.
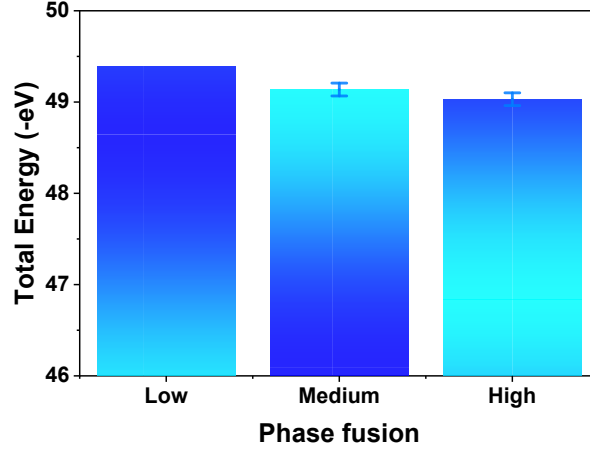
Figure S27. The calculated total electronic energy as a function of the extent of phase fusion.

The system energy difference from low fusion to high fusion is expressed by the following formula

$$\Delta H = \Delta E - T\Delta S$$

ΔH is the enthalpy change, ΔE is the energy change of the system, T is the temperature, and ΔS is the enthalpy change.

The configuration entropy (S_{config}) can be calculated according to the Boltzmann formula (*Phys. Rep., 2006,426,1-45*).

$$S_{config} = k_B \ln \Omega$$

where k_B is the Boltzmann constant and Ω is the total number of all microstructures in a specific macroscopic state.

$$S_{max} = k_B \ln \left(\frac{N!}{\left(\frac{1}{6}N\right)! \left(\frac{1}{6}N\right)! \left(\frac{1}{6}N\right)! \left(\frac{1}{2}N\right)!} \right) \approx Nk_B ln2\sqrt{3} = N * 0.107 meV/K$$

where N is the number of the unit cell. Thus, the maximum change of free energy caused by entropy at 1100 °C is about 0.16 eV. This magnitude is on the same order as the energy changes among the structures with different degrees of phase fusion. It is rational that the high temperature can drive the local structural changes.

The SQS algorithm can be described as the following steps:

(1) Read in an initial lattice structure from a file.

(2) Calculate the expected neighbor distribution (END) of the initial lattice.

(3) Set the END as the target distribution.

(4) Randomly select two atoms of different types from the lattice.

(5) Attempt to swap the atom types.

(6) Recalculate the END and measure the difference from the target.

15

(7) Accept the swap if it reduces the difference based on Metropolis criteria.

(8) Repeat steps 4-7 via Monte Carlo to explore configurations.

(9) Periodically check if the END has converged to the target within a tolerance.

(10) Continue Monte Carlo steps until convergence or maximum steps reached.

(11) The final structure matches the target END, representing an effectively random configuration constrained by the initial END.

(12) Output the SQS for characterization of its structural properties versus the initial lattice. Electronic structure calculations could then be performed on the SQS and initial structures for comparison to assess impact of randomization.

(13) Varying generation parameters may optimize the SQS representation of the realistic material.
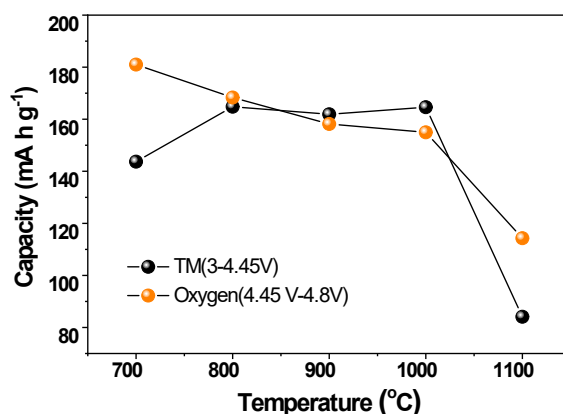
Figure S28. Contribution of capacities in different voltage regions during the first cycle of charging.
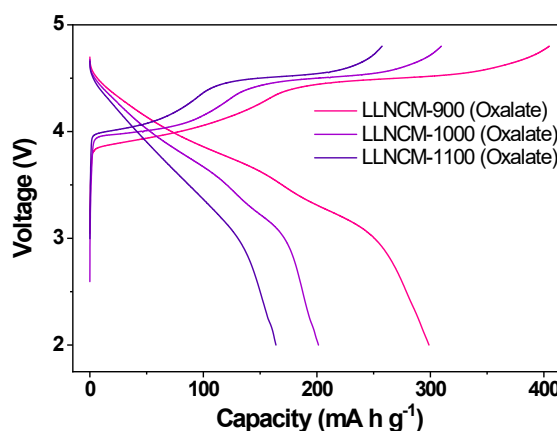
Figure S29. The 1st capacity-voltage profiles of LLNCM-900, LLNCM-1000 and LLNCM-1100 cathodes synthesized using the oxalate method.

To check whether the synthetic method of precursors affect the electrochemical performance, we used another oxalate precipitation method to conduct experiments (Synthesis details shown as below) and found that the electrochemical curves of LLNCM-900, LLNCM-1000, and LLNCM-1100 showed a similar trend of capacity decline with those prepared by the sol-gel method. It may indicate that the synthetic method of precursors would not change the trend in the structure evolution during the subsequent calcination.

The amounts of raw materials required are calculated based on 0.05 mol $0.5Li[Li_{1/3}Mn_{2/3}]O_2 \cdot 0.5Li[Ni_{1/3}Co_{1/3}Mn_{1/3}]O_2$ (3 % excess of lithium). Nickel acetate tetrahydrate ($NiAc_2 \cdot 4H_2O$) was added in 16 g of water and stirred until fully dissolved. Lithium acetate dihydrate ($LiAc \cdot 2H_2O$) and manganese acetate tetrahydrate ($MnAc_2 \cdot 4H_2O$) were then added and dissolved completely. 80 g of ethanol was added and stirred until a homogeneous mixed salt solution was obtained. Oxalic acid dihydrate ($H_2C_2O_4 \cdot 2H_2O$) was dissolved in 50 g of ethanol to form an oxalic acid solution. The mixed salt solution was placed in a 90 °C oil bath, and then the oxalic acid solution was rapidly added dropwise into the mixed salt solution using a pipette under rigorous stirring. The powder obtained after drying was collected and ground uniformly. It was then calcined at 500 °C for 3 hours in a muffle furnace. The resulting powder was ground thoroughly to ensure homogeneity. Similar with the sol-gel method, subsequent calcination was performed on samples with the same calcination temperatures and times to obtain LLNCM-900, LLNCM-1000 and LLNCM-1100, respectively.
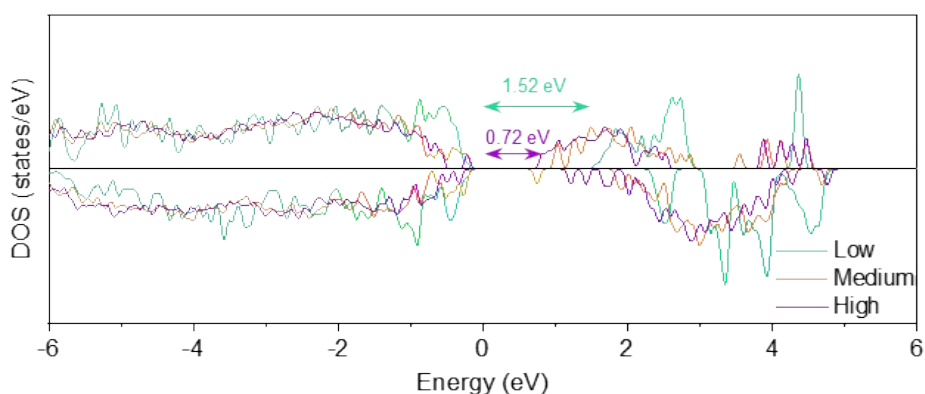
Figure S30. Total density of states (DOS) for low, medium, and high fusion structure.

Figure S30 illustrates that the band gap between the conduction band and the Fermi level (E_f) in the total density of states narrows from 1.72 eV to 0.72 eV upon increasing the degree of fusion. This reduction suggests an enhancement in electrical conductivity and potentially improved cycling performance.
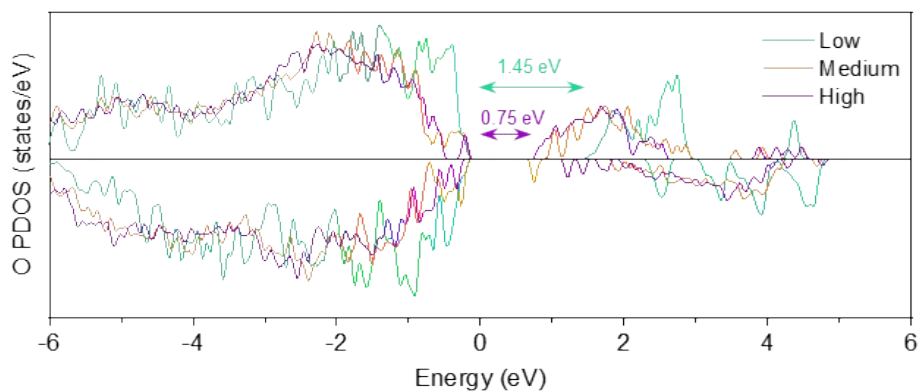
Figure S31. Projected density of states (PDOS) of O 2*p* for low, medium, and high fusion structure.
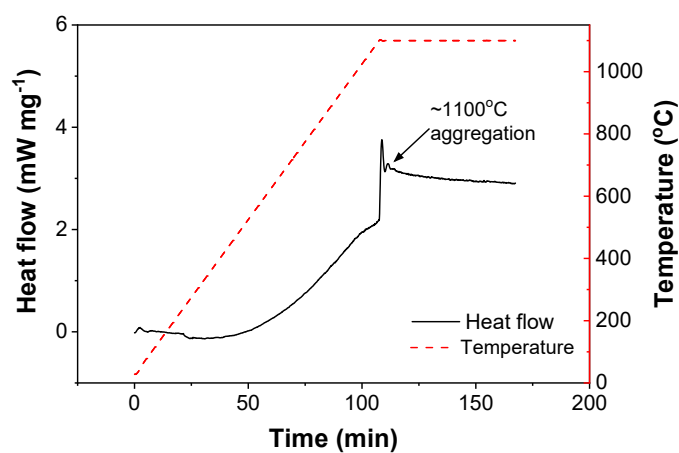
Figure S32. DSC scan on the mixture of Li_2MnO_3 and NCM111 cathodes.

According to your suggestion, we mixed monoclinic (Li_2MnO_3) and rhombohedral (NCM111) phases together in a molar ratio of 1:1 and performed DSC tests. As shown in Figure S33, there is a sharp endothermal peak when holding at 1100 °C, which may correlate with the solid solution reaction.
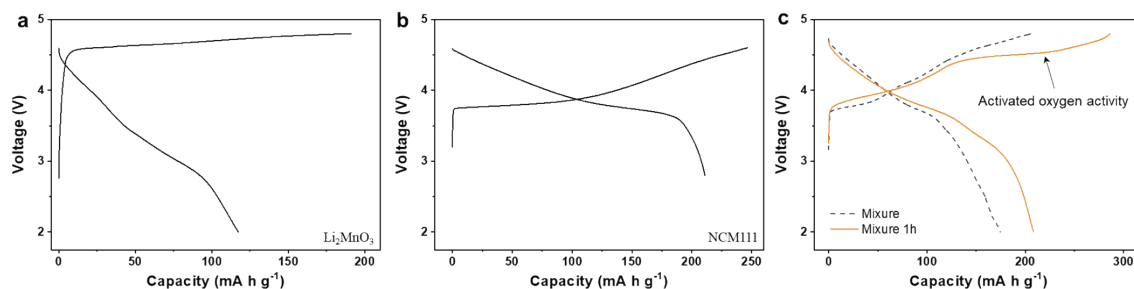
Figure S33. First cycle voltage-specific capacity curves of **a** Li_2MnO_3 **b** NCM111 and **c** two kinds of mixtures. One kind is the simple mixing of Li_2MnO_3 and NCM111 in a molar ratio of 1:1 (labeled as Mixture). The other kind is obtained by sealing the first kind of Mixture in a glass tube and calcining at 1100 ℃ for 1 hour.

We mixed Li_2MnO_3 and NCM111 in a molar ratio of 1:1, then sealed the mixture in a quartz tube with Ar atmosphere and performed calcination at 1100°C for 1 hour (Mixture 1h). The first charge/discharge curves for Li_2MnO_3, NCM111 and the mixture before and after the calcination were compared in Figure S33. The results demonstrate that at 1100 ℃, interparticle elemental diffusion was achieved. This is significant because Li_2MnO_3 has traditionally been regarded as oxygen inert. However, upon sealing and sintering a tube of the material at 1100°C for 1 hour, reversible oxygen activity was observed (Figure S33). The results indicate sintering at 1100°C could affect the local structure and thus the oxygen redox chemistry. Therefore, the judgment of the phase fusion degree is valid above 900 ℃.
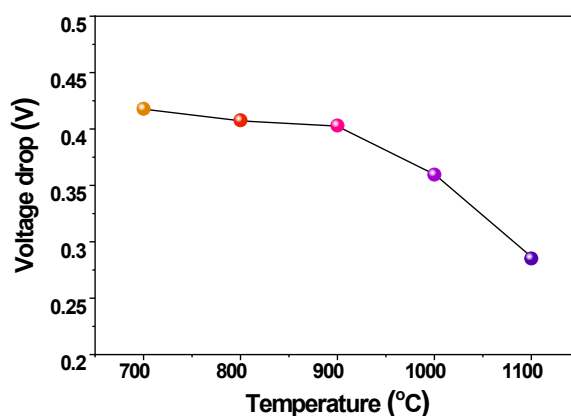
Figure S34. The average voltage drop after 50 cycles.
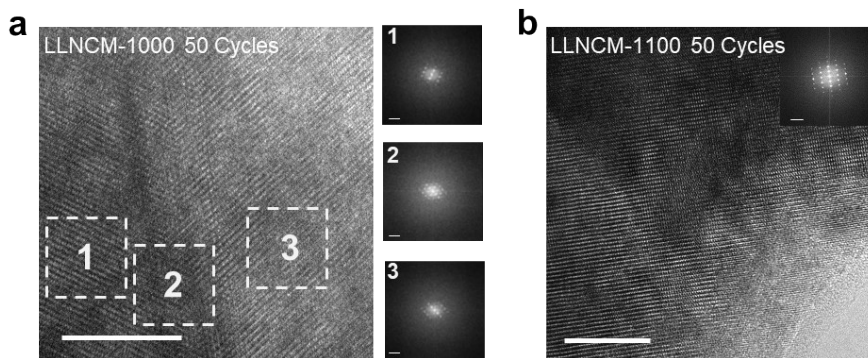
Figure S35. HRTEM images of LLNCM-1000 (a) and LLNCM-1100 after cycling. The scale bars in HRTEM images and FFT maps are 5 nm and 5 1/nm, respectively.
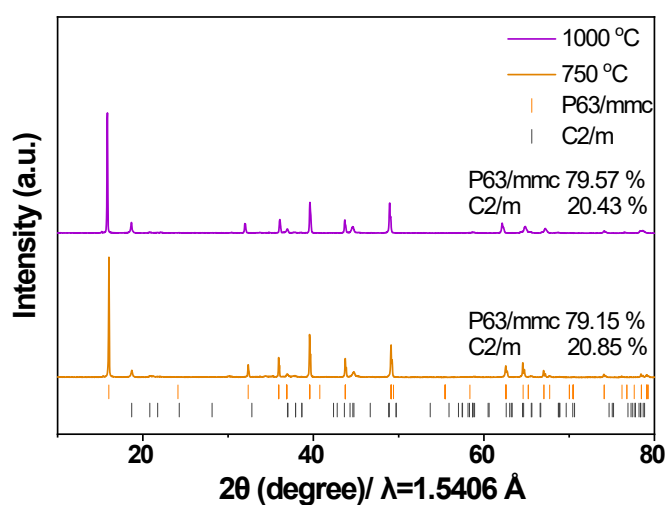
Figure S36. The XRD patterns of the layered cathode $Na_{0.67}Li_{0.25}Mn_{0.63}Ni_{0.21}Al_{0.06}O_2$ synthesized at different temperautres. Rietveld refinements show the similar phase compositions for these two samples.

The amounts of raw materials required are calculated based on 0.01 mol $Na_{0.67}Li_{0.25}Mn_{0.63}Ni_{0.21}Al_{0.06}O_2$ (2 % excess of sodium) obtained by a sol-gel method and a subsequent low-temperature sintering. In a typical process, 4.9533 g $CH_3COONa \cdot 3H_2O$ (Aladdin, 100 %, 3 % excess), 0.2576 g $CH_3COOLi \cdot 2H_2O$ (Aladdin, 99 %), 0.5278 g $(CH_3COO)_2Ni \cdot 4H_2O$ (Aladdin, 99 %), 1.5597 g $(CH_3COO)_2Mn \cdot 4H_2O$ (Aladdin, 99 %) and 0.0982 g $Al(NO_3)_3 \cdot 9H_2O$ (Aladdin, 99 %) in the stoichiometric ratio were mixed in 100 mL deionized water. 2 g polyvinylpyrrolidone (Aladdin, K30) were added as the chelating agents. The solution was dried at 90 °C, and then the powder was calcined at 140 °C for 3 hours and 500 °C for 3 hours to obtain the precursor. The precursor (0.2 g) was calcined at 750 and 1000 °C for 12 hours, respectively.

Table S1. ICP-OES test results of LLNCM-700, LLNCM-800, LLNCM-900, LLNCM-1000 and LLNCM-1100 cathodes.

Samples	LLNCM-700	LLNCM-800	LLNCM-900	LLNCM-1000	LLNCM-1100
Li Content (atom %)	54.73	55.00	55.07	55.76	55.07
TM content (atom %)	45.27	45.00	44.93	44.24	44.93

Inductively coupled plasma optical emission spectrometer (ICP-OES) analysis confirmed that 5 samples exhibited essentially consistent lithium content 55 %, validating our approach of varied holding time to compensate for temperature effects on lithium retention. This validation was important to reliably interpret comparative measurements amongst samples experiencing different thermal histories.

Table S2. The detailed structural parameters obtained from the refinement results in Figure. S16.

Temperature	Rwp (%)	Phases	Phase fraction (%)	a (Å)	b (Å)	c (Å)	β (°)
700 ℃	7.51	R-3m	74.69(99)	2.8511(13)	—	14.1968(98)	—
		C2/m	25.31(99)	4.9920(97)	8.526(17)	4.9778(78)	109.37(17)
800 ℃	4.63	R-3m	80.5(69)	2.8496(57)	—	14.2137(29)	—
		C2/m	19.5(69)	5.1822(70)	8.573(24)	5.0340(68)	109.85(20)
900 ℃	11.14	R-3m	94.39(69)	2.8489(92)	—	14.2096(67)	—
		C2/m	5.61(69)	5.0474(28)	8.3872016(10)	5.0389 (15)	109.92 (47)
1000 ℃	7.10	R-3m	95.90(77)	2.8530(10)	—	14.2298(50)	—
		C2/m	4.10(77)	4.9622(32)	8.6295(61)	5.0179(30)	109.54(66)
1100 ℃	11.41	R-3m	100	2.8517(83)	—	14.2301(58)	—

Table S3. Three different refinement results for XRD pattern of LLNCM-1000.

Number	R-3m Phase fraction (%)	Rwp	a	c
1	100	9.6	2.852713 (12)	14.22862 (6)
2	95.9 (8)	7.1	2.852982 (8)	14.22980 (4)
3	71.5 (8)	7.2	2.851567 (4)	14.22957 (2)

Table S4. Atomic parameters in three different refinements above.

Number	1		2		3	
Atom	Occupy	Beq	Occupy	Beq	Occupy	Beq
Ni1	0.02989	1.822	0.02785	2.033	0.0145	0.9449
Li1	0.9701	1.822	0.9721	2.033	0.9855	0.9449
Li2	0.02989	0.5474	0.02785	0.5499	0.0145	0.6705
Ni2	0.3031	0.5474	0.3051	0.5499	0.3185	0.6705
O1	1	0.1	1	0.1	1	0.1
Co1	0.333	0.5474	0.333	0.5499	0.333	0.6705
Mn1	0.333	0.5474	0.333	0.5499	0.333	0.6705

Table S5. Quantitative analysis of stacking fault features in samples.

Temperature (°C)	Alpha 0104	Standard Deviation	Stacking faults probability (%)
700	0.58519	0.00334	62.22 (50)
800	0.64017	0.004	53.97(60)
900	0.72541	0.00108	41.19 (16)
1000	0.87443	0.00066	18.83 (10)
1100	0.85557	0.00141	21.66 (21)

Table S6. The detailed structural parameters obtained from the PDF refinement results in Figure S22.

Temperature (°C)	a (Å)	b (Å)	c (Å)
700	2.8632 (88)	2.8632 (88)	14.127 (120)
800	2.8625 (92)	2.8625 (92)	14.155 (130)
900	2.8618 (79)	2.8618 (79)	14.181 (120)
1000	2.8630 (79)	2.8630 (79)	14.178 (120)
1100	2.87789 (85)	2.8779 (85)	14.183 (120)

Table S7. The detailed O positions obtained from the PDF refinement results in Figure S22.

Temperature (ºC)	O type	x	y	z
700	O1	0	0	0.2381 (16)
	O2	0	0	0.7619 (16)
	O3	0.666667	0.333333	0.5715 (16)
	O4	0.666667	0.333333	0.0952 (16)
	O5	0.333333	0.666667	0.9048 (16)
	O6	0.333333	0.666667	0.4285 (16)
800	O1	0	0	0.2385 (18)
	O2	0	0	0.7615 (18)
	O3	0.666667	0.333333	0.5718 (18)
	O4	0.666667	0.333333	0.0948 (18)
	O5	0.333333	0.666667	0.9052 (18)
	O6	0.333333	0.666667	0.4282 (18)
900	O1	0	0	0.2385 (16)
	O2	0	0	0.7614 (16)
	O3	0.666667	0.333333	0.5719 (16)
	O4	0.666667	0.333333	0.0948 (16)
	O5	0.333333	0.666667	0.9052 (16)
	O6	0.333333	0.666667	0.4281 (16)
1000	O1	0	0	0.2384 (16)
	O2	0	0	0.7616 (16)
	O3	0.666667	0.333333	0.5717 (16)
	O4	0.666667	0.333333	0.0949 (16)
	O5	0.333333	0.666667	0.9051 (16)
	O6	0.333333	0.666667	0.4283 (16)
1100	O1	0	0	0.2373 (14)
	O2	0	0	0.7627 (14)
	O3	0.666667	0.333333	0.5706 (14)
	O4	0.666667	0.333333	0.0960 (14)
	O5	0.333333	0.666667	0.9040 (14)
	O6	0.333333	0.666667	0.4297 (14)

Table S8. Local environment statistics and the corresponding probability in the medium fusion structure model of Figure S25.

Number	Ni	Mn	Co	Li	Medium fusion	Number	Ni	Mn	Co	Li	Medium fusion
1	0	0	0	6	0.0000	43	1	2	3	0	0.0208
2	0	0	1	5	0.0000	44	1	3	0	2	0.0573
3	0	0	2	4	0.0000	45	1	3	1	1	0.0469
4	0	0	3	3	0.0000	46	1	3	2	0	0.0365
5	0	0	4	2	0.0000	47	1	4	0	1	0.0052
6	0	0	5	1	0.0000	48	1	4	1	0	0.0729
7	0	0	6	0	0.0000	49	1	5	0	0	0.0417
8	0	1	0	5	0.0000	50	2	0	0	4	0.0000
9	0	1	1	4	0.0000	51	2	0	1	3	0.0000
10	0	1	2	3	0.0052	52	2	0	2	2	0.0000
11	0	1	3	2	0.0000	53	2	0	3	1	0.0000
12	0	1	4	1	0.0052	54	2	0	4	0	0.0000
13	0	1	5	0	0.0000	55	2	1	0	3	0.0000
14	0	2	0	4	0.0000	56	2	1	1	2	0.0104
15	0	2	1	3	0.0156	57	2	1	2	1	0.0156
16	0	2	2	2	0.0208	58	2	1	3	0	0.0104
17	0	2	3	1	0.0156	59	2	2	0	2	0.0313
18	0	2	4	0	0.0000	60	2	2	1	1	0.0156
19	0	3	0	3	0.0208	61	2	2	2	0	0.0417
20	0	3	1	2	0.0469	62	2	3	0	1	0.0729
21	0	3	2	1	0.0417	63	2	3	1	0	0.0156
22	0	3	3	0	0.0052	64	2	4	0	0	0.0260
23	0	4	0	2	0.0521	65	3	0	0	3	0.0000
24	0	4	1	1	0.0156	66	3	0	1	2	0.0000
25	0	4	2	0	0.0365	67	3	0	2	1	0.0052
26	0	5	0	1	0.0000	68	3	0	3	0	0.0000
27	0	5	1	0	0.0365	69	3	1	0	2	0.0000
28	0	6	0	0	0.0156	70	3	1	1	1	0.0052
29	1	0	0	5	0.0000	71	3	1	2	0	0.0000
30	1	0	1	4	0.0000	72	3	2	0	1	0.0052
31	1	0	2	3	0.0000	73	3	2	1	0	0.0156
32	1	0	3	2	0.0000	74	3	3	0	0	0.0156
33	1	0	4	1	0.0000	75	4	0	0	2	0.0000
34	1	0	5	0	0.0000	76	4	0	1	1	0.0000
35	1	1	0	4	0.0000	77	4	0	2	0	0.0000
36	1	1	1	3	0.0000	78	4	1	0	1	0.0000
37	1	1	2	2	0.0000	79	4	1	1	0	0.0000
38	1	1	3	1	0.0052	80	4	2	0	0	0.0000
39	1	1	4	0	0.0052	81	5	0	0	1	0.0000
40	1	2	0	3	0.0313	82	5	0	1	0	0.0000
41	1	2	1	2	0.0313	83	5	1	0	0	0.0000
42	1	2	2	1	0.0260	84	6	0	0	0	0.0000

Table S9. Local environment statistics and the corresponding probability in the high fusion structure model of Figure S26.

Number	Ni	Mn	Co	Li	High fusion	Number	Ni	Mn	Co	Li	High fusion
1	0	0	0	6	0.0000	43	1	2	3	0	0.0052
2	0	0	1	5	0.0000	44	1	3	0	2	0.0521
3	0	0	2	4	0.0000	45	1	3	1	1	0.0729
4	0	0	3	3	0.0000	46	1	3	2	0	0.0365
5	0	0	4	2	0.0000	47	1	4	0	1	0.0729
6	0	0	5	1	0.0000	48	1	4	1	0	0.0781
7	0	0	6	0	0.0000	49	1	5	0	0	0.0260
8	0	1	0	5	0.0000	50	2	0	0	4	0.0000
9	0	1	1	4	0.0000	51	2	0	1	3	0.0000
10	0	1	2	3	0.0000	52	2	0	2	2	0.0000
11	0	1	3	2	0.0000	53	2	0	3	1	0.0000
12	0	1	4	1	0.0000	54	2	0	4	0	0.0000
13	0	1	5	0	0.0000	55	2	1	0	3	0.0000
14	0	2	0	4	0.0000	56	2	1	1	2	0.0208
15	0	2	1	3	0.0000	57	2	1	2	1	0.0208
16	0	2	2	2	0.0208	58	2	1	3	0	0.0000
17	0	2	3	1	0.0104	59	2	2	0	2	0.0208
18	0	2	4	0	0.0000	60	2	2	1	1	0.0469
19	0	3	0	3	0.0000	61	2	2	2	0	0.0156
20	0	3	1	2	0.0573	62	2	3	0	1	0.0260
21	0	3	2	1	0.0365	63	2	3	1	0	0.0365
22	0	3	3	0	0.0052	64	2	4	0	0	0.0156
23	0	4	0	2	0.0365	65	3	0	0	3	0.0000
24	0	4	1	1	0.0573	66	3	0	1	2	0.0052
25	0	4	2	0	0.0156	67	3	0	2	1	0.0052
26	0	5	0	1	0.0208	68	3	0	3	0	0.0000
27	0	5	1	0	0.0260	69	3	1	0	2	0.0000
28	0	6	0	0	0.0000	70	3	1	1	1	0.0052
29	1	0	0	5	0.0000	71	3	1	2	0	0.0000
30	1	0	1	4	0.0000	72	3	2	0	1	0.0156
31	1	0	2	3	0.0000	73	3	2	1	0	0.0104
32	1	0	3	2	0.0000	74	3	3	0	0	0.0000
33	1	0	4	1	0.0000	75	4	0	0	2	0.0000
34	1	0	5	0	0.0000	76	4	0	1	1	0.0000
35	1	1	0	4	0.0000	77	4	0	2	0	0.0000
36	1	1	1	3	0.0000	78	4	1	0	1	0.0000
37	1	1	2	2	0.0156	79	4	1	1	0	0.0000
38	1	1	3	1	0.0104	80	4	2	0	0	0.0000
39	1	1	4	0	0.0000	81	5	0	0	1	0.0000
40	1	2	0	3	0.0000	82	5	0	1	0	0.0000
41	1	2	1	2	0.0417	83	5	1	0	0	0.0000
42	1	2	2	1	0.0573	84	6	0	0	0	0.0000

Table S10. Local environment statistics and the corresponding probability in solid solution model.

Number	Ni	Mn	Co	Li	Solid solution	Number	Ni	Mn	Co	Li	Solid solution
1	0	0	0	6	0.0000	43	1	2	3	0	0.0116
2	0	0	1	5	0.0001	44	1	3	0	2	0.0347
3	0	0	2	4	0.0003	45	1	3	1	1	0.0694
4	0	0	3	3	0.0004	46	1	3	2	0	0.0347
5	0	0	4	2	0.0003	47	1	4	0	1	0.0521
6	0	0	5	1	0.0001	48	1	4	1	0	0.0521
7	0	0	6	0	0.0000	49	1	5	0	0	0.0313
8	0	1	0	5	0.0004	50	2	0	0	4	0.0003
9	0	1	1	4	0.0019	51	2	0	1	3	0.0013
10	0	1	2	3	0.0039	52	2	0	2	2	0.0019
11	0	1	3	2	0.0039	53	2	0	3	1	0.0013
12	0	1	4	1	0.0019	54	2	0	4	0	0.0003
13	0	1	5	0	0.0004	55	2	1	0	3	0.0039
14	0	2	0	4	0.0029	56	2	1	1	2	0.0116
15	0	2	1	3	0.0116	57	2	1	2	1	0.0116
16	0	2	2	2	0.0174	58	2	1	3	0	0.0039
17	0	2	3	1	0.0116	59	2	2	0	2	0.0174
18	0	2	4	0	0.0029	60	2	2	1	1	0.0347
19	0	3	0	3	0.0116	61	2	2	2	0	0.0174
20	0	3	1	2	0.0347	62	2	3	0	1	0.0347
21	0	3	2	1	0.0347	63	2	3	1	0	0.0347
22	0	3	3	0	0.0116	64	2	4	0	0	0.0260
23	0	4	0	2	0.0260	65	3	0	0	3	0.0004
24	0	4	1	1	0.0521	66	3	0	1	2	0.0013
25	0	4	2	0	0.0260	67	3	0	2	1	0.0013
26	0	5	0	1	0.0313	68	3	0	3	0	0.0004
27	0	5	1	0	0.0313	69	3	1	0	2	0.0039
28	0	6	0	0	0.0156	70	3	1	1	1	0.0077
29	1	0	0	5	0.0001	71	3	1	2	0	0.0039
30	1	0	1	4	0.0006	72	3	2	0	1	0.0116
31	1	0	2	3	0.0013	73	3	2	1	0	0.0116
32	1	0	3	2	0.0013	74	3	3	0	0	0.0116
33	1	0	4	1	0.0006	75	4	0	0	2	0.0003
34	1	0	5	0	0.0001	76	4	0	1	1	0.0006
35	1	1	0	4	0.0019	77	4	0	2	0	0.0003
36	1	1	1	3	0.0077	78	4	1	0	1	0.0019
37	1	1	2	2	0.0116	79	4	1	1	0	0.0019
38	1	1	3	1	0.0077	80	4	2	0	0	0.0029
39	1	1	4	0	0.0019	81	5	0	0	1	0.0001
40	1	2	0	3	0.0116	82	5	0	1	0	0.0001
41	1	2	1	2	0.0347	83	5	1	0	0	0.0004
42	1	2	2	1	0.0347	84	6	0	0	0	0.0000

References

1. T. Matsunaga, H. Komatsu, K. Shimoda, T. Minato, M. Yonemura, T. Kamiyama, S. Kobayashi, T. Kato, T. Hirayama, Y. Ikuhara, H. Arai, Y. Ukyo, Y. Uchimoto and Z. Ogumi, *Chem. Mater.*, 2016, 28, 4143–4150.
2. M. H. Lee, Y. J. Kang, S. T. Myung and Y. K. Sun, *Electrochim. Acta*, 2004, 50, 939–948.
3. M. V. Reddy, G. V. S. Rao and B. V. R. Chowdari, *J. Power Sources*, 2006, 159, 263–267.
4. I. Belharouak, Y. K. Sun, J. Liu and K. Amine, *J. Power Sources*, 2003, 123, 247–252.
5. M. Gu, I. Belharouak, A. Genc, Z. Wang, D. Wang, K. Amine, F. Gao, G. Zhou, S. Thevuthasan, D. R. Baer, J.-G. Zhang, N. D. Browning, J. Liu and C. Wang, *Nano Lett.*, 2012, 12, 5186–5191.
6. Y. Duan, L. Yang, M.-J. Zhang, Z. Chen, J. Bai, K. Amine, F. Pan and F. Wang, *J. Mater. Chem. A*, 2019, 7, 513–519.